JGR Space Physics

RESEARCH ARTICLE
10.1029/2022JA031002

Investigation of the Southern Hemisphere Mid-High Latitude Thermospheric $\sum O/N_2$ Responses to the Space-X Storm

Xuguang Cai[1], Wenbin Wang[2], Dong Lin[2], Richard W. Eastes[1], Liying Qian[2], Qingyu Zhu[2], J. Correira[3], William E. McClintock[1], Quan Gan[1], Saurav Aryal[1], F. I. Laskar[1], and D. K. Karan[1]

[1]Laboratory for Atmospheric and Space Physics, University of Colorado Boulder, Boulder, CO, USA, [2]High Altitude Observatory, National Center for Atmospheric Research, Boulder, CO, USA, [3]Computational Physics, Inc., Springfield, VA, USA

Key Points:

- Global-scale Observations of the Limb and Disk (GOLD) observed a southern hemisphere $\sum O/N_2$ depletion on the east side of its field-of-view (local afternoon)
- The GOLD observed southern $\sum O/N_2$ is different from the classical theory of the thermosphere composition response to geomagnetic storms
- Simulation shows that the observed $\sum O/N_2$ depletion is generated in local morning, and transported equatorward, corotated to later local times

Supporting Information:

Supporting Information may be found in the online version of this article.

Correspondence to:

X. Cai,
Xuguang.Cai@colorado.edu

Citation:

Cai, X., Wang, W., Lin, D., Eastes, R. W., Qian, L., Zhu, Q., et al. (2023). Investigation of the Southern Hemisphere mid-high latitude thermospheric $\sum O/N_2$ responses to the Space-X storm. *Journal of Geophysical Research: Space Physics*, *128*, e2022JA031002. https://doi.org/10.1029/2022JA031002

Received 12 SEP 2022
Accepted 21 FEB 2023

Author Contributions:

Conceptualization: Xuguang Cai, Wenbin Wang
Data curation: Xuguang Cai
Formal analysis: Xuguang Cai
Funding acquisition: Wenbin Wang, Richard W. Eastes, William E. McClintock
Investigation: Xuguang Cai
Methodology: Xuguang Cai, Wenbin Wang

Abstract The geomagnetic storm on February 3, 2022 caused the loss of 38 Starlink satellites of Space-X. The Global-scale Observations of the Limb and Disk (GOLD) observations and Multi-Scale Atmosphere Geospace Environment (MAGE) model simulations are utilized to investigate the thermospheric composition responses to the Space-X storm. The percentage difference of the GOLD observed thermospheric O and N_2 column density ratio ($\sum O/N_2$) between the storm time (February 3, Day-of-Year [DOY] 34) and quiet time (DOY 32) shows a depletion region in the local noon sector mid-high latitudes in the southern hemisphere, which corresponds to the east side of GOLD field-of-view (FOV). This is different from the classic theory of thermospheric composition disturbance during geomagnetic storms, under which the $\sum O/N_2$ depletion is usually generated at local midnight and high latitudes, and thus, appear on the west side of GOLD FOV. MAGE simulations reproduce the observations qualitatively and indicate that the $\sum O/N_2$ depletion is formed due to strong upwelling in the local morning caused by strong Joule heating. Interestingly, enhanced equatorward winds appear near local midnight, but also in the local morning sector, which transports $\sum O/N_2$ depletion equatorward. The depletion corotates toward the local afternoon and is observed in the GOLD FOV. The equatorward winds in the local morning are due to the ion-neutral coupling under the conditions of a dominant positive interplanetary magnetic field east-west component (B_y) during the storm.

1. Introduction

The response of thermosphere composition to geomagnetic storms has been explored for several decades since the pioneering work by Seaton (1956). Based on the observations from satellite-borne gas analyzers and numerical modeling, Prölss (1980, 1981) and Burns et al. (1991) summarized how the thermospheric composition responds to geomagnetic storms. When a storm begins, enhanced Joule heating produces neutral temperature gradients in the polar region. Consequently, a composition disturbance is generated due to upwelling or downwelling associated with temperature gradients and wind divergence/convergence. Furthermore, the neutral composition disturbance is usually formed near local midnight at high-latitudes and then transported equatorward to mid and even low latitudes by horizontal advection due to enhanced equatorward winds. Meanwhile, it corotates from the local midnight into the local morning sector. This theory has been validated by numerous observational and modeling studies (e.g., Burns et al., 1992, 1995, 2006; Cai et al., 2020; Cai, Burns, Wang, Qian, Solomon, et al., 2021; Fuller-Rowell et al., 1994, 1996; Yu, Cai, et al., 2022; Yu, Wang, Ren, Cai, et al., 2021; Yu, Wang, Ren, Yue, et al., 2021).

The column density ratio of atomic Oxygen (O) to molecular Nitrogen (N_2) ($\sum O/N_2$) is an important thermospheric parameter that can be derived from the observed OI 135.6 nm and N_2 Lyman-Birge-Hopfield (LBH) emission radiances (Strickland et al., 1995, 1999, 2001). $\sum O/N_2$ is calculated by integrating densities of O and N_2 from infinity down to an altitude where the column number density of N_2 equals to $1 \times 10^{17}/cm^2$. Therefore, it is actually defined on a constant pressure surface with no altitude information (Correira et al., 2021). Due to the exponential decrease of O and N_2 number densities with altitude, O and N_2 between 140 and 180 km mostly consist of the $1 \times 10^{17}/cm^2$ N_2 column number density. $\sum O/N_2$ can be used to represent the variations of thermosphere composition due to geomagnetic disturbances (Burns et al., 1995; Cai et al., 2020; Cai, Burns, Wang, Qian, Solomon, et al., 2021; Cai, Burns, Wang, Qian, Pedatella, et al., 2021; Crowley et al., 2006; Kil et al., 2011; Meier et al., 2005; Y. Zhang et al., 2003). Moreover, $\sum O/N_2$ is also crucial for understanding the

Project Administration: Wenbin Wang, Richard W. Eastes
Software: Xuguang Cai, Dong Lin
Supervision: Wenbin Wang, Richard W. Eastes
Validation: Xuguang Cai
Visualization: Xuguang Cai, Dong Lin, Qingyu Zhu
Writing – original draft: Xuguang Cai
Writing – review & editing: Xuguang Cai, Wenbin Wang, Dong Lin, Richard W. Eastes, Liying Qian, Qingyu Zhu, J. Correira, William E. McClintock, Quan Gan, Saurav Aryal, F. I. Laskar, D. K. Karan

ionosphere responses to geomagnetic disturbances (Aa et al., 2022; C. S. Lin et al., 2022; Liou et al., 2005; Lu et al., 2012; Meier et al., 2005; Verkhoglyadova et al., 2017; Zhai, Cai, et al., 2023; Zhai, Tang, et al., 2023; Y. Zhang et al., 2003) since it reflects the production and loss of the ionospheric F-region plasma (Rishbeth, 1998). Additionally, O and N_2 are two of the major components of the thermosphere, influencing the total mass density of the thermosphere, which is important for monitoring and predicting the drag force of low-Earth-orbiting satellites (Dietrich et al., 2022).

The hemispheric asymmetry in solar irradiance (during non-equinoctial periods), asymmetric offset between the geographic and geomagnetic axes in the two hemispheres and non-dipolar terms of the geomagnetic field (Förster & Cnossen, 2013; Laundal et al., 2017) produce hemispheric differences in the momentum and heating sources in the upper atmosphere, which result in significant interhemispheric differences in the thermosphere and ionosphere responses to geomagnetic disturbances (Astafyeva et al., 2020; Hong et al., 2021; Knipp et al., 2021; Wang et al., 2021; Zhu et al., 2022). Notably, the mechanisms of thermospheric composition responses to geomagnetic storms were mainly based on the limited observations in the northern hemisphere (Burns et al., 1991, 1995; Prölss, 1980, 2011). There are fewer studies of thermospheric composition responses to geomagnetic storms in the southern hemisphere (Immel et al., 2001; Yu, Wang, Ren, Cai, et al., 2021), and the composition patterns reported in these studies are still consistent with the theory of storm-time composition disturbance proposed by Prölss (1980, 1981, 2011). A question then arises: can composition response to geomagnetic storms in the southern hemisphere be different from that in the northern hemisphere? If yes, what is the mechanism? The two-dimensional (2D) synoptic imaging of $\sum O/N_2$ from the Global-scale Observations of the Limb and Disk (GOLD) mission in geostationary orbit allows for the study on the middle thermosphere composition responses to geomagnetic storms in the southern hemisphere. In this paper, we report the responses of the $\sum O/N_2$ in mid-high latitudes of the southern hemisphere to the geomagnetic storm that occurred on February 3, 2022, which resulted in the loss of the newly launched 38 small satellites from Space-X (Fang et al., 2022; Hapgood et al., 2022; D. Lin et al., 2022; Y. Zhang et al., 2022). The $\sum O/N_2$ simulated by the Multi-Scale Atmosphere Geospace Environment (MAGE) model from the Center for Geospace Storms (D. Lin et al., 2021) displays a similar pattern to that observed by GOLD. Therefore, the MAGE outputs are utilized to investigate the underlying physical mechanisms of the southern hemisphere $\sum O/N_2$ responses to the geomagnetic storm. The remainder of this paper is organized as follows. Section 2 describes the observation data and numerical model. Section 3 provides results, including data-model comparison and model diagnostic. Section 4 gives the discussion, and the conclusions are presented in Section 5.

2. Data and Model

2.1. GOLD Data

GOLD is onboard the SES-14 communication satellite, which was launched on January 25, 2018. The satellite is in a geostationary orbit over 47.5°W. The only scientific instrument onboard is the GOLD Far Ultraviolet (FUV) imager, which performs measurements in the Far-Ultraviolet spectrum (Eastes et al., 2017, 2020). As the instrument makes measurements from geostationary orbit, GOLD provides airglow images of the same geographic region (70°S–70°N, 120°W–20°E) in a similar universal time (UT) range (06:10–00:25 UT of the next day) every day. It observes Earth's airglow emissions from 134 to ∼162 nm, including the OI 135.6 nm and N_2 LBH bands from 140.0 to 150.0 nm during the daytime with a spectral resolution of 0.2 nm and OI 135.6 nm radiance at night with a spectral resolution of 0.35 nm (Cai, Burns, Wang, Qian, Liu, et al., 2021; Eastes et al., 2017; Laskar et al., 2021; Qian et al., 2022). $\sum O/N_2$ is derived from the daytime OI 135.6 nm and N_2 LBH brightness. For the daytime mode, the GOLD imager scans the full disk at a cadence of 2 hr (08:10–18:10 UT). In this study, we utilized the GOLD observed $\sum O/N_2$ in the southern hemisphere with a spatial resolution of 2° × 2°. The measurement errors of the $\sum O/N_2$ data are 5%–10% (Correira et al., 2021; Eastes et al., 2020).

2.2. Multi-Scale Atmosphere Geospace Environment

MAGE is a newly developed geospace model that can resolve and study the mesoscale structures during geomagnetic storms, such as subauroral polarization stream (D. Lin et al., 2021) and traveling atmospheric disturbance (Pham et al., 2022). The MAGE configuration used in the present study couples the Grid Agnostic Magnetohydrodynamic (MHD) for Extended Research Applications (GAMERA) global MHD model of the magnetosphere

(Sorathia et al., 2020; B. Zhang, Sorathia, Lyon, Merkin, Garretson, et al., 2019), the Rice Convection Model (RCM) of the ring current (Toffoletto et al., 2003), Thermosphere Ionosphere Electrodynamics General Circulation Model (TIEGCM) (Qian et al., 2014; Richmond et al., 1992; Roble et al., 1988), and the RE-developed Magnetosphere-Ionosphere Coupler/Solver (REMIX) (Merkin & Lyon, 2010). GAMERA is a new MHD model based on the algorithms underlying the Lyon-Fedder-Mobarry model (Lyon et al., 2004).

In this study, GAMERA employs 96 × 96 × 128 grid cells in the radial, meridional, and azimuthal directions, respectively, where the spherical symmetry axis of the grid is pointing from Earth to Sun. The radial grid spacing is ~0.2R_E near the inner boundary, which is set at 1.5R_E. RCM uses 180 × 360 × 140 grid cells in the latitudinal, longitudinal (in Solar Magnetic [SM] coordinates), and energy dimensions, respectively. The RCM grid has a resolution of 0.25° × 1° in latitude and longitude, respectively. In the energy dimension, there are 34 energy channels for electrons, 105 energy channels for protons, and 1 zero-energy channel for the cold plasmasphere. The energy invariants of these channels correspond to electron kinetic energy of ~10 eV to ~10 keV and ion kinetic energy of 10 eV–~100 keV at the geosynchronous orbit. The energy grid has a good coverage of the typical energy range of ions consisting of the ring current and electrons that contribute to the diffuse electron precipitation. REMIX grid uses 45×360 grid cells in the latitudinal and longitudinal directions (in SM coordinates), respectively. Its resolution is 1.0° in both dimensions and the low latitude boundary is at 45° magnetic latitude (MLAT). The resolution of TIEGCM is 1.25°latitude × 1.25°longitude × 0.25 scale height. GAMERA and TIEGCM both adopt a ring-average technique to treat the singularity at the spherical axes of their respective grids (B. Zhang, Sorathia, Lyon, Merkin, & Wiltberger, 2019). GAMERA and RCM exchange information every 10 s, GAMERA and REMIX every 5 s, and REMIX and TIEGCM every 5s. The lower boundary of TIEGCM is the monthly tidal climatology described in Hagan and Forbes (2002, 2003) without accounting for day-to-day tidal variability. The output thermosphere and ionosphere parameters are in a 5-min temporal cadence.

3. Results

3.1. Geomagnetic Conditions

Figure 1 shows the (a) *K*p index and the solar radio flux at 10.7 cm (F10.7), (b) solar wind speed, (c) interplanetary magnetic field (IMF) west-east component (B_y) and north-south component (B_z), and (d) the disturbance storm time index (Dst) between Day-of-Year (DOY) 32 and 36 in 2022. *K*p was less than 2 before 20:00 UT and suddenly increased from 0^+ to 3^+ after 21:00 UT on DOY 32. It reached a maximum of 4 on DOY 33 and increased to a maximum of 5^+ at 09:00 UT on DOY 34. It subsequently fluctuated between 3^- and 5^+ until the end of DOY 36. Although the geomagnetic disturbance ended on DOY 40 (not shown here), we focus on DOY 32 to 34 in this paper. The F10.7 index varied from 124.9 to 122.9 between DOY 32 and 34. Therefore, the influence of solar irradiance variations on the thermospheric composition should be negligible during this storm. As shown in Figure 1b, the solar wind speed decreased from 452 to 338 km/s and then suddenly increased to 512 km/s at 23:00 UT on DOY 32. On DOY 33, solar wind speed fluctuated between 380 and 480 km/s. It reached a maximum of 580 km/s at 14:05 UT on DOY 34. As shown in Figure 1c, B_y and B_z fluctuated between −3 and 6 nT before 22:00 UT on DOY 32. Before DOY 34, there were two major southward turnings of B_z that occurred at 22:50 UT on DOY 32 and 14:40 UT on DOY 33. Since 00:55 UT on DOY 34, B_z began to decrease from 8.96 nT and turned southward at 02:10 UT. It decreased to −18.56 nT at 09:35 UT on DOY 34. B_y was ~10–13 nT between 00:55 and 07:35 UT on DOY 34, suggesting a period of dominant positive B_y. B_y decreased from 10.55 nT at 07:35 UT to −16 nT at 11:35 UT. Dst was between −10 and 15 nT during DOY 32 and 33, and suddenly decreased from 6 nT at 00:00 UT on DOY 34 to reach a minimum of −66 nT at 10:00 UT on DOY 34. The variations of geomagnetic indices show that the geomagnetic disturbance started at the end of DOY 32, and the storm began at 00:00 UT on DOY 34. DOY 32 is chosen as the reference quiet day because it is the only relatively quiet day (*K*p < 2 most of the time) between DOY 25 and 36. Although there were geomagnetic disturbances after 21:00 UT on DOY 32, the observations that will be discussed are between 00:00 and 19:00 UT on DOY 34. The corresponding reference time range (00:00–19:00 UT on DOY 32) is still quiet.

3.2. Data-Model Comparison

The $\sum O/N_2$ percentage difference between DOY 34 and 32 is calculated by subtracting $\sum O/N_2$ on DOY 32 from $\sum O/N_2$ on DOY 34 and divided by $\sum O/N_2$ on DOY 32, which reflects the relative variations of $\sum O/N_2$ on DOY

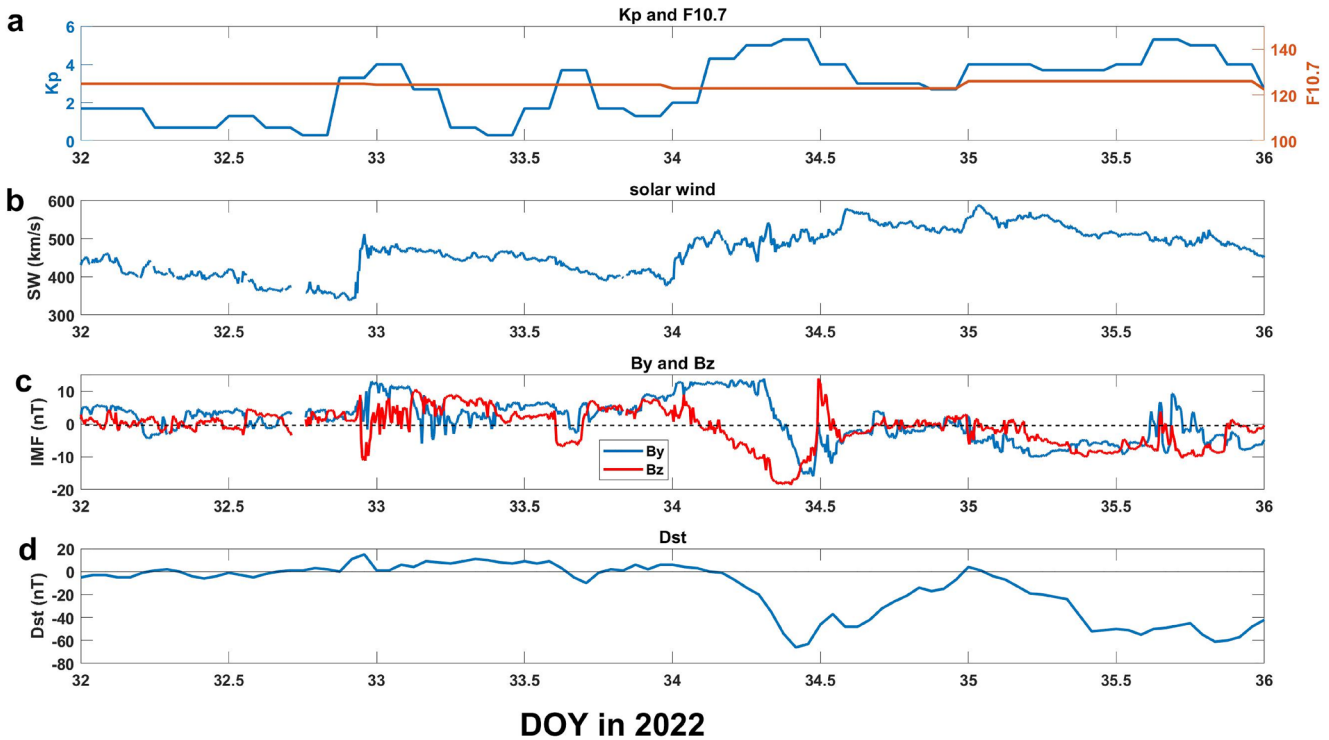

Figure 1. Temporal evolution of (a) *Kp* (blue) and F10.7 (red), (b) solar wind speed, (c) interplanetary magnetic field (IMF) B_y (blue) and B_z (red), and (d) Dst between Day-of-Year (DOY) 32 and 36 in 2022. Dotted line in (c) and black line in (d) stand for the zero line.

34 (disturbed day) compared with that on DOY 32 (reference quiet day). When the percentage difference is negative, we use "depletion" to describe that $\sum O/N_2$ on DOY 34 is smaller than that on DOY 32. When the percentage difference is positive, we use "enhancement" to describe that $\sum O/N_2$ on DOY 34 is larger than that on DOY 32.

Figure 2 shows the (left column) GOLD observed and (right column) MAGE simulated percentage differences of $\sum O/N_2$ between DOY 34 and 32 in the southern hemisphere (20°S–70°S, 120°W–30°E in geographic coordinate) at 10:20, 12:20, 14:20, and 16:20 UT. The reference altitude of N_2 column density of $10^{17}/cm^2$ in the model is around 135–140 km. The *X*-axis is the longitude with the corresponding local time (LT). MAGE simulation results are displayed within the GOLD field-of-view (FOV). As shown in Figure 2, there is an $\sum O/N_2$ depletion region on the eastside of GOLD FOV at 10:20 UT (08:20–10:20 LT). The magnitude is ∼20% and the latitude range is between 45°S and 60°S. From 10:20 to 14:20 UT, this depletion region moves westward and expands equatorward. Its magnitude increases to 30% and its geographic range expands into 60°W to 0, and 40°S to 70°S. At 16:20 UT, the depletion region becomes smaller. For MAGE simulation, there is an $\sum O/N_2$ depletion region on the east side of GOLF FOV, as well. The depletion region also moves westward between 10:20 and 14:20 UT, and subsequently stays roughly in the same latitude-longitude region. The magnitude of this simulated depletion is larger (∼40%). In addition, there is an $\sum O/N_2$ enhancement between 20°S and 40°S, 90°W and 30°W in the GOLD FOV. But the corresponding simulated $\sum O/N_2$ enhancement is between 40°S and 70°S. There is also a depletion on the west side of GOLD FOV between 40°S and 20°S in the simulated $\sum O/N_2$, while there is no depletion seen in the corresponding observation periods (10:20–14:20 UT). These model-data discrepancies might be attributed to the differences between the real geomagnetic forcing and the simulated geomagnetic forcing in MAGE, as well as the thermosphere day-to-day variability caused by the lower atmospheric wave forcing. Although MAGE cannot reproduce all the observed $\sum O/N_2$ patterns, it simulated well the temporal evolution of the mid-high latitudes $\sum O/N_2$ depletion on the east side of GOLD FOV.

For GOLD daytime observations, between 08:10 and 18:10 UT, the local daytime sector ($\sum O/N_2$ data is available only during the daytime) in the GOLD FOV (120°W–20°E) moves from east to west. For most of the previously reported GOLD $\sum O/N_2$ responses to geomagnetic disturbances, $\sum O/N_2$ depletion appears in the local morning at mid-high latitudes, and thus on the west side of GOLD FOV, or penetrates more equatorward on the west side

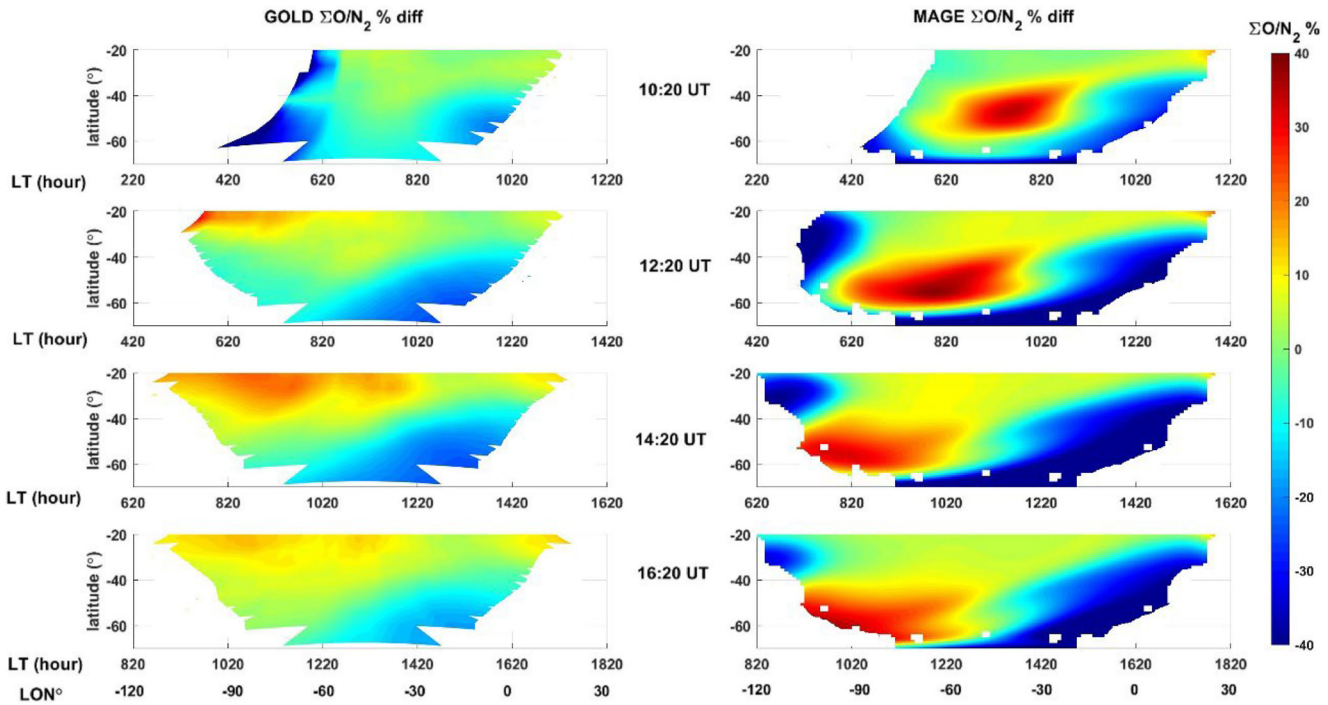

Figure 2. $\Sigma O/N_2$ percentage difference between Day-of-Year (DOY) 32 and 34 (left column) observed by Global-scale Observations of the Limb and Disk (GOLD) and (right column) simulated by Multi-Scale Atmosphere Geospace Environment (MAGE). MAGE results are modified to match with GOLD field-of-view. The longitude and the corresponding local time are given as the *x*-axis.

(Cai et al., 2020; Cai, Burns, Wang, Qian, Pedatella, et al., 2021; Cai et al., 2022; Yu, Cai, et al., 2022). Figure S1 in Supporting Information S1 shows the percentage difference of GOLD observed $\sum O/N_2$ between DOY 34 and 32 at 14:10 UT in the northern hemisphere. The depletion area penetrates more equatorward in the westside of GOLD FOV. This is consistent with the theory proposed by Prölss (1980, 2011), namely the composition disturbance is generated near local midnight and corotates from the nightside (near local midnight) into the dayside (morning). However, the $\sum O/N_2$ disturbance in Figure 2 appears to originate from local daytime, which is different from these previous results. Since the model reproduces this phenomenon qualitatively, the model output can be utilized to investigate the mechanism.

3.3. Temporal Evolution of the Simulated $\sum O/N_2$

Figure 3 shows the model-simulated $\sum O/N_2$ percentage differences between DOY 34 and 32 in the southern hemisphere (20°−90°S) from 00:20 to 13:20 UT on DOY 34 in the polar view (geographic coordinate; perimeter boundary 20°S). The GOLD FOV is marked in Figure 3f with a white line (covering 6–15 LT). The temporal evolution of the $\sum O/N_2$ percentage differences between DOY 34 and 32 in the southern hemisphere from 00:20 to 18:20 UT with 15-min cadence is shown in Movie S1. At 00:20 UT (Figure 3a), there are already two $\sum O/N_2$ depletion regions (one near 40°–60°S, 16 LT, another near 40°–60°S, 2–4 LT), as well as enhancements in the mid-high latitude, which are formed on DOY 33. Notice that in the polar region, there is a region of weak $\sum O/N_2$ depletion. At 02:20 UT (Figure 3b), the depletion in the polar region expands more equatorward in the local morning sector (5–8 LT) than the post-midnight (0–4 LT). Movie S1 shows that this $\sum O/N_2$ depletion in the polar region (70°–90°S) starts to expand at 00:20 UT. At 04:20 UT (Figure 3c), the depletion developed in both the local morning and midnight sectors. As shown in Figure 3d, the $\sum O/N_2$ depletion region merges into a single large area of $\sum O/N_2$, which expands equatorward in both local midnight and morning sectors. At 10:20 UT (Figure 3e), the $\sum O/N_2$ depletion in the local morning expands to ~40°S and corotates toward local noon (10–14 LT). Note that the $\sum O/N_2$ depletion region gradually corotates into the GOLD FOV (white lines in Figure 3f), as shown in Figure 2. The depletion in the midnight sector also moves equatorward and expands to the LT sector between 22 and 4 LT. As shown in Figure 3f (13:20 UT), the depletion formed in the local morning extends to

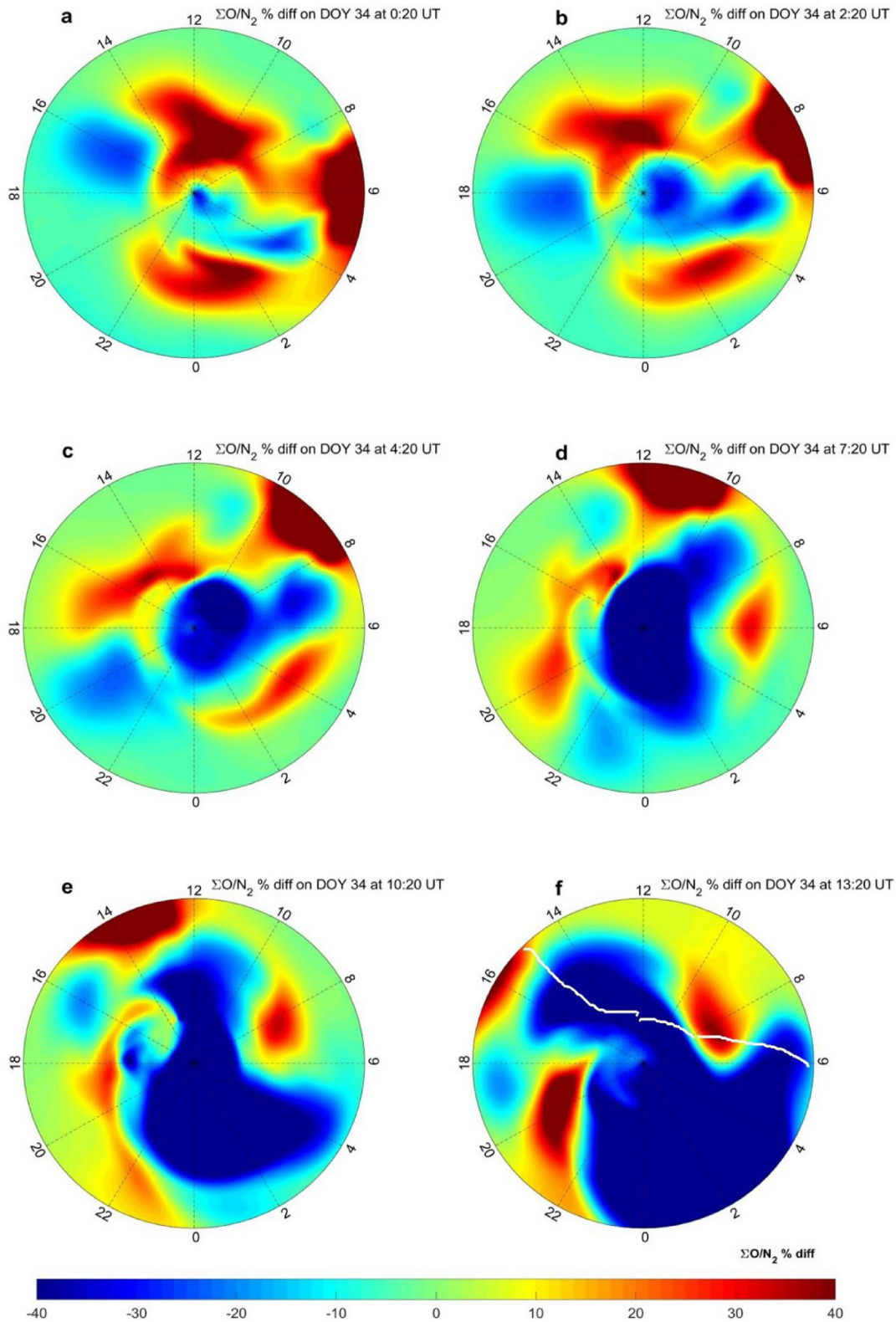

Figure 3. Polar view of the $\Sigma O/N_2$ percentage difference between DOY 32 and 34 in the southern hemisphere (geographic coordinate) at (a) 0:20, (b) 2:20, (c) 4:20, (d) 7:20, (e) 10:20, and (f) 13:20 universal time (UT). The perimeter latitude is 20°S. The white line at 3f outlines the GOLD FOV.

~30°S and corotates to the local afternoon (12–16 LT). While the depletion formed in the local midnight is not observed by GOLD, it keeps expanding toward 20°S and corotates toward local morning (7 LT).

Therefore, Figure 3 and Movie S1 show that the $\sum O/N_2$ depletion observed on the east side of GOLD FOV originates from the local morning sector near 80°S from 00:20 UT on DOY 34, and is transported to mid and low latitudes, as well as corotates to later LT sectors. Note that the polar view of the thermospheric composition disturbance in Prölss (2011) is in magnetic local time (MLT) and magnetic latitude (MLAT) frame (fig. 12 of the paper). To check whether there are significant differences between LT and MLT polar view, the corresponding simulated $\sum O/N_2$ percentage difference between DOY 34 and 32 in MLT is shown in Figures S2 and S3 in Supporting Information S1. The $\sum O/N_2$ depletion in LT and geographic coordinate is more toward local morning, while the one in MLT and MLAT is more toward post-midnight. However, the LT/MLT difference of the distribution of $\sum O/N_2$ disturbance is at most less than 2 hr. At 7:20 UT (Figure S3 in Supporting Information S1), both $\sum O/N_2$ disturbances in LT and MLT exhibit two depletion regions equatorward, one in midnight and another in local morning. Therefore, we can say that the $\sum O/N_2$ depletion in the southern hemisphere reported here (occurring in the local daytime (east side of GOLD FOV) and corotating) is different from Prölss theory (Prölss, 1980, 2011). The thermosphere composition disturbance also forms in the local morning and moves equatorward, like the one generating near local midnight. However, the classical theory only predicts that the disturbance is generated and moved equatorward near the local midnight sector. Since the observation is in geographic coordinate, the following polar view of the thermosphere and ionosphere parameters will also be presented in geographic coordinate.

3.4. Neutral Temperature and Wind Variations Related to $\sum O/N_2$ Depletion

Figure 4 shows the polar view of the southern hemisphere (geographic coordinate) neutral temperature (TN) near pressure level −1.375 (~160 km) at the same UTs as Figure 3 on DOY 34 with a perimeter latitude of 50°S. The corresponding horizontal winds are overplotted as black arrows. This pressure level is chosen because it is the composition between 140 and 180 km that determines the magnitude of $\sum O/N_2$. As shown in Figures 4a–4d, large TN enhancements occur first in the local morning sectors and move toward the local noon (from 8 LT at 00:20 UT to 12:45 LT at 07:20 UT). The maximum TN values increase from 930K at 00:20 UT to 1,160K at 07:20 UT. At 10:20 UT, the maximum TN reaches 1,380K near 11:20 LT. The TN maximum decreases to 1,060K near 8 LT at 13:20 UT. Comparisons with Figures 4a–4d indicate that there are more large regions with TN > 1,000K in Figures 4e and 4f. This is because TN is an accumulated effect of the Joule heating, solar radiation, heat conduction, horizontal and vertical heat advection, heating from chemistry reactions, adiabatic heating/cooling, and radiative cooling due to nitric oxide (NO) and carbon dioxide (CO_2) (Killeen et al., 1997). Additionally, Joule heating plays a major role in determining the polar region TN. During DOY 34, there is continuous occurrence of geomagnetic disturbances (see Figure 1a) and Joule heating is enhanced persistently. Consequently, TN in the whole polar region increases from 00:20 to 13:20 UT DOY 34.

As shown in Figure 4a, horizontal neutral winds are equatorward between 2 and 6 LT from 50°S to 90°S. From 22 to 2 LT, latitude range of equatorward winds expands from 75°S to 90°S to 50°S and 90°S. However, the latitude range of westward wind shrinks from 80°S to 40°S to 50°S and 40°S. The maximum speed of equatorward wind occurs near 23:00 LT with a magnitude of ~380 m/s. Winds are poleward and westward between 6:00 and 12:00 LT. In Figure 4b at 02:20 UT, the equatorward wind expands to 7:20 LT. The magnitude of the maximum equatorward wind increases to 500 m/s. Poleward and eastward winds are seen between 8 and 14 LT. At 04:20 UT, the equatorward winds expand to 10:00 LT. From 07:20 UT, the LT sector with equatorward winds in the morning and noon separates from the equatorward wind near the midnight sector. There is an LT sector with westward winds and weak equatorward winds in the middle of the two LT sectors with the equatorward winds. This LT sector varies between 4 and 6 LT at 07:20 UT, and between 8 and 12 LT at 13:20 UT. As shown in Figures 4d–4f, the magnitudes of equatorward wind in the local noon are smaller than the ones near local midnight. The magnitudes of the former are 100–200 m/s, while the magnitudes of the latter are 300–400 m/s at the same latitudes. Figure S4 in Supporting Information S1 shows the corresponding vertical wind (WN) near ~160 km. Since TN maximum is in the local morning between 00:20 and 07:20 UT, the maximum upward WN is also generated in this LT sector. The maximum of upward WN increases from 6 m/s at 00:20 UT to 10 m/s at 02:20 UT and stays near 10 m/s until 10:20 UT.

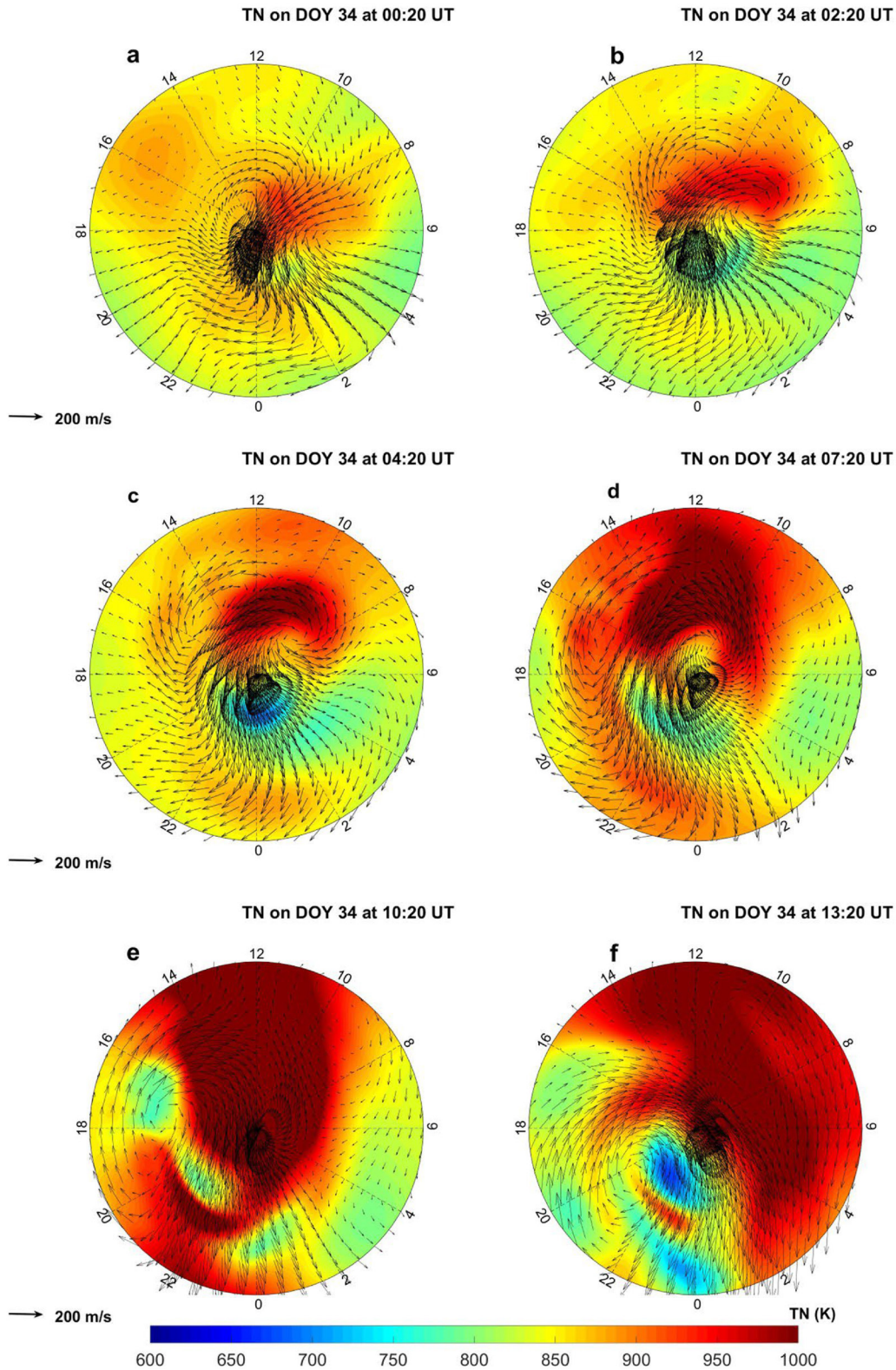

Figure 4. Polar view of the neutral temperature (TN) on Day-of-Year (DOY) 34 in the southern hemisphere (geographic coordinate) at (a) 0:20, (b) 2:20, (c) 4:20, (d) 7:20, (e) 10:20, and (f) 13:20 universal time (UT). The perimeter latitude is 50°S. The horizontal wind is overplotted in black arrows.

The neutral temperature and wind pattern are crucial in uncovering how the $\sum O/N_2$ depletion is formed and propagated. In the following, we utilize all this information to investigate the process.

4. Discussion

As already demonstrated in many previous studies, middle and upper thermosphere composition variations during storms are determined by vertical advection, horizontal advection, and molecular diffusion (Burns et al., 1989; 2006; Cai et al., 2020; Cai, Burns, Wang, Qian, Solomon, et al., 2021; Cai et al., 2022; Sutton et al., 2015; Yu, Wang, Ren, Yue, et al., 2021; Yu, Wang, Ren, Cai, et al., 2021; Yu, Wang, et al., 2022). Since diagnostic analysis of the thermosphere composition has been carried out many times in previous studies, here we do not show a detailed diagnostic process, but utilize terms in the continuity equation of thermosphere composition (see details of the equation in Burns et al., 2006; Cai, Burns, Wang, Qian, Solomon, et al., 2021; Yu, Wang, Ren, Cai, et al., 2021), as well as the aforementioned temporal evolution of TN and neutral winds to reveal the underlying mechanism of $\Sigma O/N_2$ depletion during the Space-X storms.

Oxygen (O) mmr (mass mixing ratio) increases from 100 to ~300 km, resulting in a positive vertical gradient of O mmr between 100 and ~300 km. On the other hand, N_2 mmr decreases with the increase of altitudes, and the vertical gradient of N_2 is negative. When there is upward vertical wind (upwelling), the vertical advection of O decreases the O mmr. While the vertical advection of N_2 increases the N_2 mmr. The decrease of O and increase of N_2 reduce $\sum O/N_2$ in the polar region. As shown in Figure 4 and Figure S4 in Supporting Information S1, the enhanced temperature gradient in the local morning generates an upward WN (~6–10 m/s) from 00:20 to 02:20 UT near 160 km (18–25 m/s near ~300 km, not shown here). The magnitude of WN is similar to observed high-latitude WN reported previously (10–20 m/s in Larsen & Meriwether, 2012). With the strong upward WN, $\sum O/N_2$ depletion is formed due to the vertical advection. After the depletion of $\sum O/N_2$ is formed, horizontal advection acts to transport the composition disturbance to other regions. Without the horizontal gradients of O and N_2 mmr that are partly generated by upwelling and downwelling, no horizontal advection of O and N_2 will occur. Since there is also equatorward wind in the local morning sector, the depletion is transported equatorward to mid and low latitudes. In the meantime, the depletion corotates toward later LT, which is due to the Earth's corotation and partly offset by the westward zonal wind.

Therefore, the mechanism of the generation and maintenance of $\sum O/N_2$ depletion in the southern hemisphere in the local morning sector appears to be similar to the classical theory of storm-induced composition variations. However, the major difference is that it takes place in the local morning. As shown in Figure 2, the composition disturbance is also formed in the local midnight as predicted by classical theory. But why there is also disturbance formed in the local morning in this case, which appears different from composition perturbations reported in previous studies (Prölss, 1980, 1981)? Furthermore, we need to address a related question: Why do the TN enhancement and equatorward wind occur in the local morning sector?

Figure 5 shows the polar view of the height integrated Joule heating rate (Q_{JH}) (unit: mW/m^2) in the southern hemisphere (geographic coordinate) with a perimeter latitude of 50°S at 00:20, 02:20, 04:20, 07:20, 10:20, and 13:20 UT on DOY 34. The corresponding instantaneous IMF B_y and B_z values are marked. The temporal evolution of Q_{JH} is shown in Movie S2. At 00:20 UT (Figure 5a, B_z = 2.14 nT, B_y = 12.46 nT), Q_{JH} is mainly distributed between 6 and 10 LT, 90°S and 60°S, with a maximum value of 33 mW/m^2. At 02:20 UT, with a weak southward B_z (−1.24 nT) but similar magnitude of B_y as Figure 5a, magnitude of Q_{JH} increases to 47 mW/m^2. At 04:20 (B_z = −3.12 nT, B_y = 11.87 nT) and 07:20 UT (B_z = −10.15 nT, B_y = 13.07 nT), with the increase of southward B_z, both the magnitude and latitude ranges of Q_{JH} enlarge. At 07:20 UT (Figure 5d), the maximum value of Q_{JH} reaches 50 mW/m^2. It also extends to 55°S in the local afternoon sector. The maximum Q_{JH} occurs in the local morning sector in Figures 5a–5d. At 10:20 UT, B_z is stronger than B_y. Q_{JH} increases more with the maximum (78 mW/m^2) appearing in the local afternoon. At 13:20 UT, due to smaller magnitudes of IMF B_y and B_z, Q_{JH} decreases in all high-latitude regions. Since TN is strongly influenced by Q_{JH} at high latitudes, it is the enhanced Q_{JH} in the local morning sector that generates the TN enhancements in the region. Interestingly, the magnitudes of southward IMF B_z are smaller (absolute value < 4 nT) at 0:20, 2:20, and 4:20 UTs than at 7:20, 10:20, and 13:20 UTs. However, in this time period, B_y is dominant with a magnitude of greater than 10 nT Q_{JH} is large. Therefore, even B_z is small or positive, large Q_{JH} still occurs with a dominant B_y.

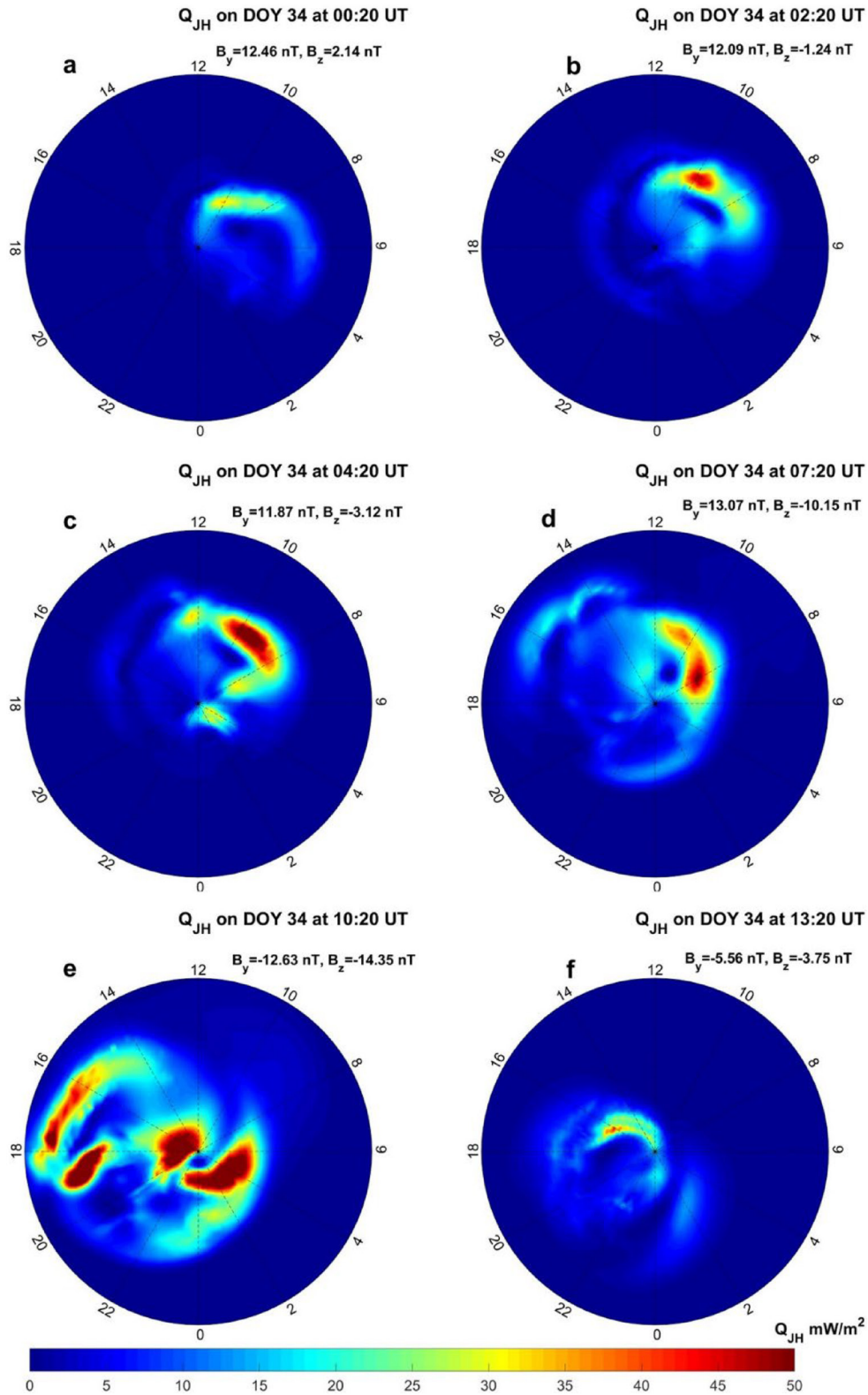

Figure 5. Polar view of the height integrated Joule heating rate (unit: mW/m^2) on Day-of-Year (DOY) 34 in the southern hemisphere (geographic coordinate) at (a) 00:20, (b) 02:20, (c) 04:20, (d) 07:20, (e) 10:20, and (f) 13:20 universal time (UT). The perimeter latitude is 50°S. Corresponding interplanetary magnetic field B_y and B_z at each UT time are marked.

Based on Knipp et al. (2004) and Lu et al. (2016), the major energy channels on thermosphere and ionosphere are solar irradiance, Joule heating, auroral precipitation, and the cusp. For auroral precipitation, it is much weaker than Joule heating (Knipp et al., 2004). Regarding cusp, it is not included in MAGE model used in this paper, but the model can still reproduce the observed $\Sigma O/N_2$ pattern. Furthermore, cusp is a local effect and mainly in the local noon (B. Zhang et al., 2012), while the formed disturbance is in the local morning. This suggests that cusp effect may also be minor compared with Joule heating. Therefore, Joule heating is the main heating source that causes the upwelling in the local morning during this storm.

To uncover why Q_{JH} is enhanced in the local morning sector, the corresponding ionospheric potential, together with the corresponding horizontal ion drift (overplotted in black arrows) at the same UTs in the southern hemisphere (geographic coordinate) is shown in Figure 6. The perimeter latitude is 50°S. As shown in Figure 6a, the maximum magnitude of dawn and dusk side potential is 68 and 11 kV, respectively, under dominant positive B_y with positive B_z. The dawn side potential is mainly between 6 and 8 LT. With a dominant positive B_y, the potential distribution is asymmetric with an orange-shaped dawn cell and banana-shaped dusk cell (Østgaard et al., 2018; Tenfjord et al., 2015). At 02:20, 04:20, and 07:20 UT (Figures 6b–6d), when B_z turns to southward with increasing magnitude but still smaller than B_y, the maximum dawn side potential increases to 85, 97, and 112 kV, while the corresponding dusk cell magnitudes are smaller. At 10:20 UT (Figure 6e), with a dominant negative B_z, the pattern becomes more symmetric than in previous UTs. At 13:20 UT, with weakened IMF, the potential magnitude drops.

It should be noted that it is summer in the southern hemisphere (February) with persistent solar radiation in the polar region. Consequently, the ionospheric conductivity is also large. This, together with the large ionospheric electric fields, generate enhanced Q_{JH} in the local morning sector during the storm, which results in the TN enhancement and upward WN in the local morning to generate $\sum O/N_2$ depletion.

The corresponding equatorward ion drifts in the dawn side also exhibit similar behavior to the potential, moving from 0 to 6 LTs toward 8–12 LTs from 00:20 to 07:20 UT. Figures S5 and S6 in Supporting Information S1 show the comparisons between the potential and horizontal ion drifts simulated by MAGE and observed by the Super Dual Auroral Radar Network (SuperDARN) (Thomas & Shepherd, 2018) at 00:20, 02:20, 04:20, and 07:20 UT. Ion drifts in both simulation and observation are equatorward in the local morning, and move toward local noon during this time period. Although there are small-scale discrepancies, the large-scale patterns are similar. The simulation reproduces the observations qualitatively. The trend of ion drifts in Figure 6 is similar to the evolution of the horizontal neutral winds shown in Figures 4a–4e, suggesting the potentially crucial roles of the ion-neutral coupling. Between 22:55 UT on DOY 33 to 07:25 UT on DOY 34, the magnetosphere was driven by a dominant positive B_y with southward B_z. As pointed out by B. Zhang et al. (2016), the convection can impact the neutral wind through ion-neutral coupling under dominant positive B_y condition in the summer hemisphere. The equatorward ion drag generates the local noon equatorward wind in the high-latitude northern hemisphere during a geomagnetically "quiet" period reported by Wu et al. (2012). For the Space-X storm conditions considered here (summer hemisphere and dominant positive B_y), the neutral winds are influenced by the equatorward ion drag in the morning to offset the day-night pressure gradient force and finally become equatorward. The detailed mechanism of the equatorward wind, including how each momentum forcing process evolves and makes contribution, will be studied in future works.

5. Conclusion

We carried out an investigation on the behavior of mid-high latitude thermosphere composition in the southern hemisphere during the Space-X storm on February 3, 2022, using GOLD $\Sigma O/N_2$ data and MAGE simulations. The main findings are as follows:

1. GOLD observed a persistent depletion region of $\Sigma O/N_2$ in the local noon, east side of its FOV during observation on DOY 34, which is different from the prediction by the classic theory of thermospheric composition response to geomagnetic storm.
2. MAGE simulations qualitatively capture the observed $\Sigma O/N_2$ depletion pattern in the southern hemisphere, though with a larger magnitude and larger area.
3. The temporal evolution of the simulated percentage difference of $\Sigma O/N_2$ illustrates that the depletion is first generated in the local morning and is transported to mid and low latitudes by the equatorward wind in the

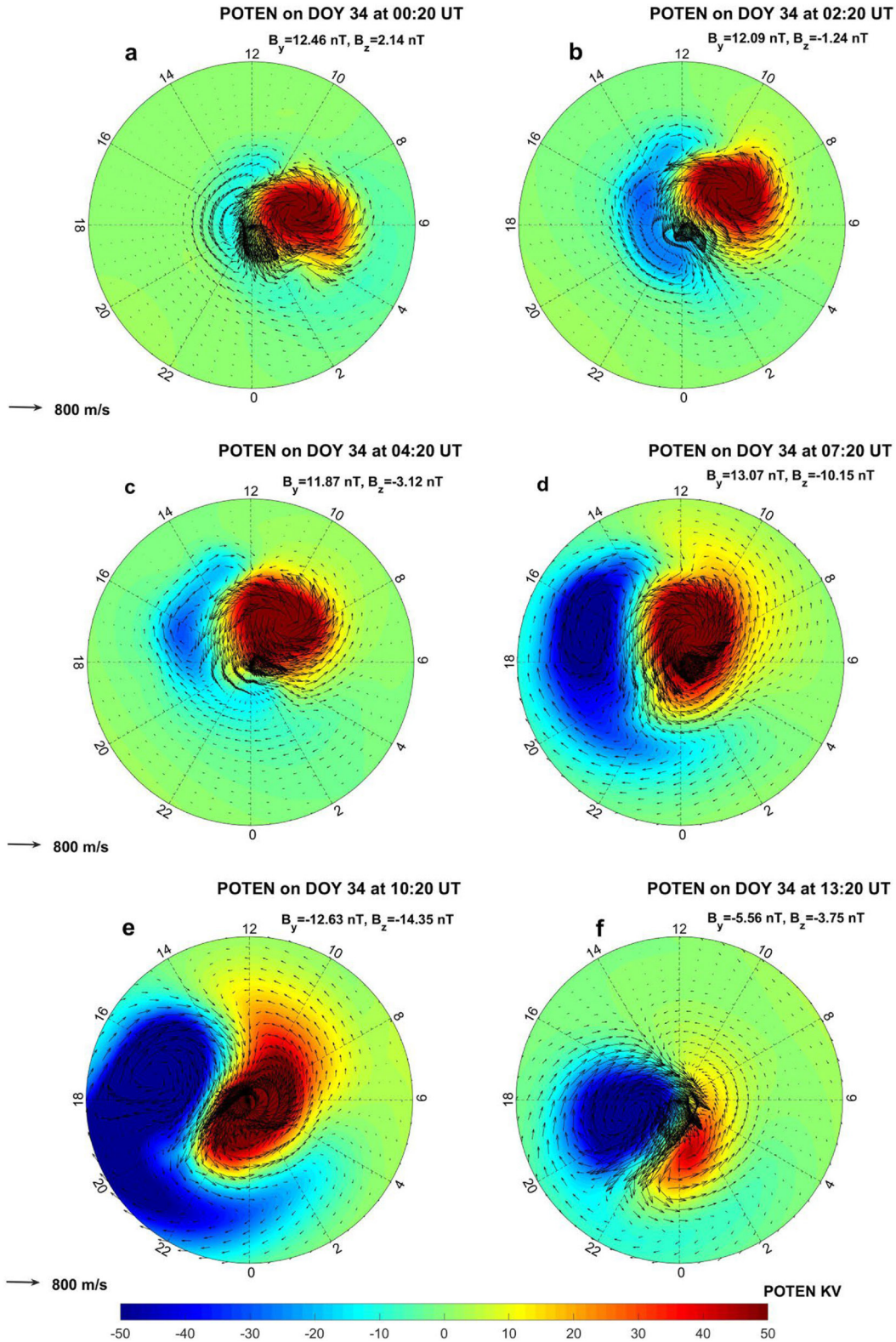

Figure 6. Polar view of the ionospheric potential on Day-of-Year (DOY) 34 in the southern hemisphere (geographic coordinate) at (a) 00:20, (b) 02:20, (c) 04:20, (d) 07:20, (e) 10:20, and (f) 13:20 universal time (UT). The perimeter latitude is 50°S. The horizontal component of ion velocity is overplotted in white arrows. Corresponding interplanetary magnetic field B_y and B_z at each UT time are marked.

local morning and noon sectors. This is different from the classical theory that the storm-time composition disturbance forms near local midnight, and then transported equatorward and corotates toward local morning.

4. The $\Sigma O/N_2$ depletion is formed at high latitudes in the local morning due to the strong upwelling, as a result of strong heating in the region. The temperature enhancement at high latitudes is formed in the local morning because of the strong Joule heating rate.
5. The ion-neutral coupling under dominant positive B_y condition is likely the cause of the equatorward wind in the local morning sector.

Data Availability Statement

The IMF and solar wind data are from https://cdaweb.gsfc.nasa.gov/cgi-bin/eval1.cgi. The F10.7 and Dst are from https://omniweb.gsfc.nasa.gov/form/dx1.html. The MAGE simulation results used to produce the figures in this paper are available at https://doi.org/10.5281/zenodo.7052115. The SuperDarn ionospheric potential and ion drift are avaliable at https://doi.org/10.5281/zenodo.7705251.

Acknowledgments
This study is supported by NASA contract 80GSFC18C0061 to the University of Colorado. This is also supported by NASA Grants NNX15AB83G, NNX17AI42G, NNX16AH06G, 80NSSC20K1350, 80NSSC20K0189, 80NSSC19K0278, 80NSSC18K0648, 80NSSC19K0835, 80NSSC20K0018, NNH19ZDA001N-HSR, NNH19ZDA001N-HGIO, NNH19ZDA001N-HTMS, NNH18ZDA001N, 80NSSC17K0013, 80NSSC20K0601, 80NSSC20K0356, 80NSSC19K0080, 80NSSC17K0679, 80NSSC21K0008, 80NSSC21K1677, and 80NSSC20K0199, and NSF CEDAR Grant 2033843. This study is also based upon work supported by the National Center for Atmospheric Research, which is a major facility sponsored by the National Science Foundation under Cooperative agreement no. 1852977. We acknolwdge the use of SuperDARN data. SuperDARN is a network of radars funded by national scientific funding agencies of Australia, Canada, China, France, Italy, Japan, Norway, South Africa, the United Kingdom and United States of America.

References

Aa, E., Zhang, S.-R., Wang, W., Erickson, P. J., Qian, L., Eastes, R., et al. (2022). Pronounced suppression and X-pattern merging of equatorial ionization anomalies after the 2022 Tonga volcano eruption. *Journal of Geophysical Research: Space Physics*, *127*(6), e2022JA030527. https://doi.org/10.1029/2022JA030527

Astafyeva, E., Bagiya, M. S., Förster, M., & Nishitani, N. (2020). Unprecedented hemispheric asymmetries during a surprise ionospheric storm: A game of drivers. *Journal of Geophysical Research: Space Physics*, *125*(3), e2019JA027261. https://doi.org/10.1029/2019JA027261

Burns, A. G., Killeen, T. L., Deng, W., Carignan, G. R., & Roble, R. G. (1995). Geomagnetic storm effects in the low- to middle-latitude upper thermosphere. *Journal of Geophysical Research*, *100*(A8), 14673. https://doi.org/10.1029/94ja03232

Burns, A. G., Killeen, T. L., & Roble, R. G. (1989). Processes responsible for the compositional structure of the thermosphere. *Journal of Geophysical Research*, *94*, 3670–3686. https://doi.org/10.1029/ja094ia04p03670

Burns, A. G., Killeen, T. L., & Roble, R. G. (1991). A theoretical study of thermospheric composition perturbations during an impulsive geomagnetic storm. *Journal of Geophysical Research: Space Physics*, *96*(A8), 14153–14167. https://doi.org/10.1029/91ja00678

Burns, A. G., Killeen, T. L., & Roble, R. G. (1992). A simulation of the thermospheric composition changes seen during a geomagnetic storm. *Advances in Space Research*, *12*, 253–256.

Burns, A. G., Wang, W., Killeen, T. L., Solomon, S. C., & Wiltberger, M. (2006). Vertical variations in the N_2 mass mixing ratio during a thermospheric storm that have been simulated using a coupled magnetosphere-ionosphere-thermosphere model. *Journal of Geophysical Research: Space Physics*, *111*(11), 1–14. https://doi.org/10.1029/2006JA011746

Cai, X., Burns, A. G., Wang, W., Qian, L., Liu, J., Solomon, S. C., et al. (2021). Observation of postsunset OI 135.6 nm radiance enhancement over South America by the GOLD mission. *Journal of Geophysical Research: Space Physics*, *126*(2), e2020JA028108. https://doi.org/10.1029/2020JA028108

Cai, X., Burns, A. G., Wang, W., Qian, L., Pedatella, N., Coster, A., et al. (2021). Variations in thermosphere composition and ionosphere total electron content under "geomagnetically quiet" conditions at solar-minimum. *Geophysical Research Letters*, *48*(11), e2021GL093300. https://doi.org/10.1029/2021GL093300

Cai, X., Burns, A. G., Wang, W., Qian, L., Solomon, S. C., Eastes, R. W., et al. (2020). The two-dimensional evolution of thermospheric ΣO/N2 response to weak geomagnetic activity during solar-minimum observed by GOLD. *Geophysical Research Letters*, *47*(18), e2020GL088838. https://doi.org/10.1029/2020GL088838

Cai, X., Burns, A. G., Wang, W., Qian, L., Solomon, S. C., Eastes, R. W., et al. (2021). Investigation of a neutral "tongue" observed by GOLD during the geomagnetic storm on May 11, 2019. *Journal of Geophysical Research: Space Physics*, *126*(6), e2020JA028817. https://doi.org/10.1029/2020JA028817

Cai, X., Wang, W., Burns, A., Qian, L., & Eastes, R. W. (2022). The effects of IMF B_y on the middle thermosphere during a geomagnetically "quiet" period at solar minimum. *Journal of Geophysical Research: Space Physics*, *127*(5), e2021JA029816. https://doi.org/10.1029/2021JA029816

Correira, J., Evans, J. S., Lumpe, J. D., Krywonos, A., Daniell, R., Veibell, V., et al. (2021). Thermospheric composition and solar EUV flux from the Global-scale Observations of the Limb and Disk (GOLD) mission. *Journal of Geophysical Research: Space Physics*, *126*(12), e2021JA029517. https://doi.org/10.1029/2021JA029517

Crowley, G., Hackert, C. L., Meier, R. R., Strickland, D. J., Paxton, L. J., Pi, X., et al. (2006). Global thermosphere-ionosphere response to onset of 20 November 2003 magnetic storm. *Journal of Geophysical Research*, *111*(A10), A10S18. https://doi.org/10.1029/2005JA011518

Dietrich, N., Matsuo, T., & Hsu, C.-T. (2022). Specifying satellite drag through coupled thermosphere-ionosphere data assimilation of radio occultation electron density profiles. *Space Weather*, *20*(8), e2022SW003147. https://doi.org/10.1029/2022SW003147

Eastes, R. W., McClintock, W. E., Burns, A. G., Anderson, D. N., Andersson, L., Aryal, S., et al. (2020). Initial observations by the Global-scale Observations of the Limb and Disk (GOLD) mission. *Journal of Geophysical Research: Space Physics*, *125*(7), e2020JA027823. https://doi.org/10.1029/2020JA027823

Eastes, R. W., McClintock, W. E., Burns, A. G., Anderson, D. N., Andersson, L., Codrescu, M., et al. (2017). The Global-scale Observations of the Limb and Disk (GOLD) mission. *Space Science Reviews*, *212*(1–2), 383–408. https://doi.org/10.1007/s11214-017-0392-2

Fang, T. W., Kubaryk, A., Goldstein, D., Li, Z., Fuller-Rowell, T., Millward, G., et al. (2022). Space weather environment during the SpaceX Starlink satellite loss in February 2022. *Space Weather*, *20*(11), e2022SW003193 Portico. https://doi.org/10.1029/2022sw003193

Förster, M., & Cnossen, I. (2013). Upper atmosphere differences between northern and southern high latitudes: The role of magnetic field asymmetry. *Journal of Geophysical Research: Space Physics*, *118*(9), 5951–5966. https://doi.org/10.1002/jgra.50554

Fuller-Rowell, T. J., Codrescu, M. V., Moffett, R. J., & Quegan, S. (1994). Response of the thermosphere and ionosphere to geomagnetic storms. *Journal of Geophysical Research*, *99*(A3), 3893–3914. https://doi.org/10.1029/93ja02015

Fuller-Rowell, T. J., Codrescu, M. V., Rishbeth, H., Moffett, R. J., & Quegan, S. (1996). On the seasonal response of the thermosphere and ionosphere to geomagnetic storms. *Journal of Geophysical Research*, *101*(A2), 2343–2353. https://doi.org/10.1029/95ja01614

Hagan, M. E., & Forbes, J. M. (2002). Migrating and nonmigrating diurnal tides in the middle and upper atmosphere excited by tropospheric latent heat release. *Journal of Geophysical Research*, *107*(D24), 4754. https://doi.org/10.1029/2001JD001236

Hagan, M. E., & Forbes, J. M. (2003). Migrating and nonmigrating semidiurnal tides in the upper atmosphere excited by tropospheric latent heat release. *Journal of Geophysical Research*, *108*(A2), 1062. https://doi.org/10.1029/2002JA009466

Hapgood, M., Liu, H., & Lugaz, N. (2022). SpaceX—Sailing close to the space weather? *Space Weather*, *20*(3), e2022SW003074. https://doi.org/10.1029/2022SW003074

Hong, Y., Deng, Y., Zhu, Q., Maute, A., Sheng, C., Welling, D., & Lopez, R. (2021). Impacts of different causes on the inter-hemispheric asymmetry of ionosphere-thermosphere system at mid- and high-latitudes: GITM simulations. *Space Weather*, *19*(11), e2021SW002856. https://doi.org/10.1029/2021SW002856

Immel, T. J., Crowley, G., Craven, J. D., & Roble, R. G. (2001). Dayside enhancement of thermospheric O/N_2 following magnetic storm onset. *Journal of Geophysical Research*, *106*(15), 471–15488. https://doi.org/10.1029/2000ja000096

Kil, H., Kwak, Y.-S., Paxton, L. J., Meier, R. R., & Zhang, Y. (2011). O and N2 disturbances in the F region during the 20 November 2003 storm seen from TIMED/GUVI. *Journal of Geophysical Research*, *116*(A2), A02314. https://doi.org/10.1029/2010JA016227

Killeen, T. L., Burns, A. G., Azeem, I., Cochran, S., & Roble, R. G. (1997). A theoretical analysis of the energy budget in the lower thermosphere. *Journal of Atmospheric and Solar-Terrestrial Physics*, *59*(6), 675–689. https://doi.org/10.1016/s1364-6826(96)00114-9

Knipp, D. J., Kilcommons, L., Hairston, M., & Coley, W. R. (2021). Hemispheric asymmetries in Poynting flux derived from DMSP spacecraft. *Geophysical Research Letters*, *48*(17), e2021GL094781. https://doi.org/10.1029/2021GL094781

Knipp, D. J., Tobiska, W. K., & Emery, B. A. (2004). Direct and indirect thermospheric heating sources for Solar Cycles 21–23. *Solar Physics*, *224*(1–2), 495–505. https://doi.org/10.1007/s11207-005-6393-4

Larsen, M. F., & Meriwether, J. W. (2012). Vertical winds in the thermosphere. *Journal of Geophysical Research*, *117*(A9), A09319. https://doi.org/10.1029/2012JA017843

Laskar, F. I., Eastes, R. W., Codrescu, M. V., Evans, J. S., Burns, A. G., Wang, W., et al. (2021). Response of GOLD retrieved thermospheric temperatures to geomagnetic activities of varying magnitudes. *Geophysical Research Letters*, *48*(15), e2021GL093905. https://doi.org/10.1029/2021GL093905

Laundal, K. M., Cnossen, I., Milan, S. E., Haaland, S. E., Coxon, J., Pedatella, N. M., et al. (2017). North-south asymmetries in Earth magnetic field. *Space Science Reviews V.*, *206*(1–4), 225–257. https://doi.org/10.1007/s11214-016-0273-0

Lin, C. S., Sutton, E. K., Wang, W., Cai, X., Liu, G., Henney, C. J., & Cooke, D. L. (2022). Satellite in-situ electron density observations of the midlatitude storm enhanced density on the noon meridional plane in the F region during the 20 November 2003 magnetic storm. *Journal of Geophysical Research: Space Physics*, *127*(5), e2021JA029831. https://doi.org/10.1029/2021JA029831

Lin, D., Sorathia, K., Wang, W., Merkin, V., Bao, S., Pham, K., et al. (2021). The role of diffuse electron precipitation in the formation of subauroral polarization streams. *Journal of Geophysical Research: Space Physics*, *126*(12), e2021JA029792. https://doi.org/10.1029/2021JA029792

Lin, D., Wang, W., Garcia-Sage, K., Yue, J., Merkin, V., McInerney, J. M., et al. (2022). Thermospheric neutral density variation during the "SpaceX" storm: Implications from physics-based whole geospace modeling. *Space Weather*, *20*(12), e2022SW003254. https://doi.org/10.1029/2022SW003254

Liou, K., Newell, P. T., Anderson, B. J., Zanetti, L., & Meng, C.-I. (2005). Neutral composition effects on ionospheric storms at middle and low latitudes. *Journal of Geophysical Research*, *110*(A5), A05309. https://doi.org/10.1029/2004JA010840

Lu, G., Goncharenko, L., Nicolls, M. J., Maute, A., Coster, A., & Paxton, L. J. (2012). Ionospheric and thermospheric variations associated with prompt penetration electric fields. *Journal of Geophysical Research*, *117*(A8), A08312. https://doi.org/10.1029/2012JA017769

Lu, G., Richmond, A. D., Lühr, H., & Paxton, L. (2016). High-latitude energy input and its impact on the thermosphere. *Journal of Geophysical Research: Space Physics*, *121*, 7108–7124. https://doi.org/10.1002/2015JA022294

Lyon, J., Fedder, J., & Mobarry, C. (2004). The Lyon-Fedder-Mobarry (LFM) global MHD magnetospheric simulation code. *Journal of Atmospheric and Solar-Terrestrial Physics*, *66*(15–16), 1333–1350. https://doi.org/10.1016/j.jastp.2004.03.020

Meier, R., Crowley, G., Strickland, D. J., Christensen, A. B., Paxton, L. J., Morrison, D., & Hackert, C. L. (2005). First look at the 20 November 2003 superstorm with TIMED/GUVI: Comparisons with a thermospheric global circulation model. *Journal of Geophysical Research*, *110*(A9), A09S41. https://doi.org/10.1029/2004JA010990

Merkin, V., & Lyon, J. (2010). Effects of the low-latitude ionospheric boundary condition on the global magnetosphere. *Journal of Geophysical Research: Space Physics*, *115*(A10), A10202. https://doi.org/10.1029/2010JA015461

Østgaard, N., Reistad, J. P., Tenfjord, P., Laundal, K. M., Rexer, T., Haaland, S. E., et al. (2018). The asymmetric geospace as displayed during the geomagnetic storm on 17 August 2001. *Annales Geophysicae*, *36*(6), 1577–1596. https://doi.org/10.5194/angeo-36-1577-2018

Pham, K. H., Zhang, B., Sorathia, K., Dang, T., Wang, W., Merkin, V., et al. (2022). Thermospheric density perturbations produced by traveling atmospheric disturbances during August 2005 storm. *Journal of Geophysical Research: Space Physics*, *127*(2), e2021JA030071. https://doi.org/10.1029/2021JA030071

Prölss, G. W. (1980). Magnetic storm associated perturbation of the upper atmosphere: Recent results obtained by satellite-borne gas analyzers. *Reviews of Geophysics*, *18*(1), 183–202. https://doi.org/10.1029/rg018i001p00183

Prölss, G. W. (1981). Latitudinal structure and extension of the polar atmospheric disturbance. *Journal of Geophysical Research*, *86*(A4), 2385–2396. https://doi.org/10.1029/ja086ia04p02385

Prölss, G. W. (2011). Density perturbations in the upper atmosphere caused by the dissipation of solar wind energy. *Surveys in Geophysics*, *32*(2), 101–195. https://doi.org/10.1007/s10712-010-9104-0

Qian, L., Emery, B. A., Foster, B., Lu, G., Maute, A., Richmond, A. D., et al. (2014). The NCAR TIE-GCM: A community model of the coupled thermosphere/ionosphere system. In J. Huba, R. Schunk, & G. Khazanov (Eds.), *Modeling the ionosphere-thermosphere system* (pp. 73–83). John Wiley. https://doi.org/10.1002/9781118704417.ch7

Qian, L., Gan, Q., Wang, W., Cai, X., Eastes, R., & Yue, J. (2022). Seasonal variation of thermospheric composition observed by NASA GOLD. *Journal of Geophysical Research: Space Physics*, *127*(6), e2022JA030496. https://doi.org/10.1029/2022JA030496

Richmond, A. D., Ridley, E. C., & Roble, R. G. (1992). A thermosphere/ionosphere general circulation model with coupled electrodynamics. *Geophysical Research Letters*, *19*(6), 601–604. https://doi.org/10.1029/92GL00401

Rishbeth, H. (1998). How the thermospheric circulation affects the ionospheric *F*2-layer. *Journal of Atmospheric and Terrestrial Physics*, *60*(14), 1385–1402. https://doi.org/10.1016/S1364-6826(98)00062-5

Roble, R. G., Ridley, E. C., Richmond, A. D., & Dickinson, R. E. (1988). A coupled thermosphere/ionosphere general circulation model. *Geophysical Research Letters*, *15*(12), 1325–1328. https://doi.org/10.1029/GL015i012p01325

Seaton, M. J. (1956). A possible explanation of the drop in F-region critical densities accompanying major ionospheric storms. *Journal of Atmospheric and Terrestrial Physics*, *8*(1–2), 122–124. https://doi.org/10.1016/0021-9169(56)90102-7

Sorathia, K., Merkin, V., Panov, E., Zhang, B., Lyon, J., Garretson, J., et al. (2020). Ballooning-interchange instability in the near-earth plasma sheet and auroral beads: Global magnetospheric modeling at the limit of the MHD approximation. *Geophysical Research Letters*, *47*(14), e2020GL088227. https://doi.org/10.1029/2020GL088227

Strickland, D. J., Bishop, J., Evans, J. S., Majeed, T., Shen, P. M., Cox, R. J., et al. (1999). Atmospheric Ultraviolet Radiance Integrated Code (AURIC): Theory, software architecture, inputs, and selected results. *Journal of Quantitative Spectroscopy & Radiative Transfer*, *62*(6), 689–742. https://doi.org/10.1016/S0022-4073(98)00098-3

Strickland, D. J., Daniell, R. E., & Craven, J. D. (2001). Negative ionospheric storm coincident with DE-1 observed thermospheric disturbance on October 14, 1981. *Journal of Geophysical Research*, *106*(A10), 21049–21062. https://doi.org/10.1029/2000JA000209

Strickland, D. J., Evans, J. S., & Paxton, L. (1995). Satellite remote sensing of thermospheric O/N_2 and solar EUV: 1. Theory. *Journal of Geophysical Research*, *100*(A7), 12217–12226. https://doi.org/10.1029/95JA00574

Sutton, E. K., Thayer, J. P., Wang, W., Solomon, S. C., Liu, X., & Foster, B. T. (2015). A self-consistent model of helium in the thermosphere. *Journal of Geophysical Research: Space Physics*, *120*, 6884–6900. https://doi.org/10.1002/2015JA021223

Tenfjord, P., stgaard, N., Snekvik, K., Laundal, K. M., Reistad, J. P., Haaland, S., & Milan, S. E. (2015). How the IMF *By* induces a *By* component in the closed magnetosphere and how it leads to asymmetric currents and convection patterns in the two hemispheres. *Journal of Geophysical Research: Space Physics*, *120*(11), 9368–9384. https://doi.org/10.1002/2015ja021579

Thomas, E. G., & Shepherd, S. G. (2018). Statistical patterns of ionospheric convection derived from mid-latitude, high-latitude, and polar SuperDARN HF radar observations. *Journal of Geophysical Research: Space Physics*, *123*(4), 3196–3216. https://doi.org/10.1002/2018JA025280

Toffoletto, F., Sazykin, S., Spiro, R., & Wolf, R. (2003). Inner magnetospheric modeling with the rice convection model. *Space Science Reviews*, *107*(1–2), 175–196. https://doi.org/10.1023/A:10255320080

Verkhoglyadova, O. P., Komjathy, A., Mannucci, A. J., Mlynczak, M. G., Hunt, L. A., & Paxton, L. J. (2017). Revisiting ionosphere-thermosphere responses to solar wind driving in superstorms of November 2003 and 2004. *Journal of Geophysical Research: Space Physics*, *122*(10), 10824–10850. https://doi.org/10.1002/2017JA024542

Wang, Z., Zou, S., Liu, L., Ren, J., & Aa, E. (2021). Hemispheric asymmetries in the mid-latitude ionosphere during the September 7–8, 2017 storm: Multi-instrument observations. *Journal of Geophysical Research: Space Physics*, *126*(4), e2020JA028829. https://doi.org/10.1029/2020JA028829

Wu, Q., Wang, W., Roble, R. G., Häggström, I., & Strømme, A. (2012). First daytime thermospheric wind observation from a balloon-borne Fabry-Perot interferometer over Kiruna (68N). *Geophysical Research Letters*, *39*(14), L14104. https://doi.org/10.1029/2012GL052533

Yu, T., Cai, X., Ren, Z., Li, S., Pedatella, N., & He, M. (2022). Investigation of the $\Sigma O/N_2$ depletion with latitudinally tilted equatorward boundary observed by GOLD during the geomagnetic storm on April 20, 2020. *Journal of Geophysical Research: Space Physics*, *127*(12), e2022JA030889. https://doi.org/10.1029/2022JA030889

Yu, T., Wang, W., Ren, Z., Cai, X., Liu, L., He, M., et al. (2022). Diagnostic analysis of the physical processes underlying the long-duration $\Sigma O/N2$ depletion during the recovery phase of the 8 June 2019 geomagnetic storm. *Journal of Geophysical Research: Space Physics*, *127*(12), e2022JA031075. https://doi.org/10.1029/2022JA031075

Yu, T., Wang, W., Ren, Z., Cai, X., Yue, X., & He, M. (2021). The response of middle thermosphere (~160 km) composition to the November 20 and 21, 2003 superstorm. *Journal of Geophysical Research: Space Physics*, *126*(10), e2021JA029449. https://doi.org/10.1029/2021JA029449

Yu, T., Wang, W., Ren, Z., Yue, J., Yue, X., & He, M. (2021). Middle-low latitude neutral composition and temperature responses to the 20 and 21 November 2003 superstorm from GUVI dayside Limb measurements. *Journal of Geophysical Research: Space Physics*, *126*(8), e2020JA028427. https://doi.org/10.1029/2020ja028427

Zhai, C., Cai, X., Wang, W., Coster, A., Qian, L., Solomon, S. C., et al. (2023). Mid-latitude ionospheric response to a weak geomagnetic activity event during solar minimum. *Journal of Geophysical Research: Space Physics*, *128*(1), e2022JA030908. https://doi.org/10.1029/2022JA030908

Zhai, C., Tang, S., Peng, W., Cheng, X., & Zheng, D. (2023). Driver of the positive ionospheric storm over the South American sector during 4 November 2021 Geomagnetic Storm. *Remote Sensing*, *15*(1), 111. https://doi.org/10.3390/rs15010111

Zhang, B., Lotko, W., Brambles, O., Wiltberger, M., Wang, W., Schmitt, P., & Lyon, J. (2012). Enhancement of thermospheric mass density by soft electron precipitation. *Geophysical Research Letters*, *39*(20), L20102. https://doi.org/10.1029/2012GL053519

Zhang, B., Sorathia, K. A., Lyon, J. G., Merkin, V. G., Garretson, J. S., & Wiltberger, M. (2019). GAMERA: A three-dimensional finite-volume MHD solver for non-orthogonal curvilinear geometries. *The Astrophysical Journal – Supplement Series*, *244*(1), 20. https://doi.org/10.3847/1538-4365/ab3a4c

Zhang, B., Sorathia, K. A., Lyon, J. G., Merkin, V. G., & Wiltberger, M. (2019). Conservative averaging-reconstruction techniques (ring average) for 3-d finite-volume MHD solvers with axis singularity. *Journal of Computational Physics*, *376*, 276–294. https://doi.org/10.1016/j.jcp.2018.08.020

Zhang, B., Wang, W., Wu, Q., Knipp, D., Kilcommons, L., Brambles, O. J., et al. (2016). Effects of magnetospheric lobe cell convection on dayside upper thermospheric winds at high latitudes. *Geophysical Research Letters*, *43*(16), 8348–8355. https://doi.org/10.1002/2016GL069834

Zhang, Y., Paxton, L. J., Kil, H., Meng, C.-I., Mende, S. B., Frey, H. U., & Immel, T. J. (2003). Negative ionospheric storms seen by the IMAGE FUV instrument. *Journal of Geophysical Research*, *108*(A9), 1343. https://doi.org/10.1029/2002JA009797

Zhang, Y., Paxton, L. J., Schaefer, R., & Swartz, W. H. (2022). Thermospheric conditions associated with the loss of 40 Starlink satellites. *Space Weather*, *20*(10), e2022SW003168 Portico. https://doi.org/10.1029/2022sw003168

Zhu, Q., Lu, G., & Deng, Y. (2022). Low- and mid-latitude ionospheric response to the 2013 St. Patrick's day geomagnetic storm in the American sector: Global ionosphere thermosphere model simulation. *Frontiers in Astronomy and Space Sciences*, *9*, 916739. https://doi.org/10.3389/fspas.2022.916739